Progress In Electromagnetics Research C, Vol. 116, 221–233, 2021

Simulation Research on Magnetoacoustic Concentration Tomography with Magnetic Induction Based on Uniaxial Anisotropy of Magnetic Nanoparticles

Xiaoheng Yan, Yuxin Hu*, Weihua Chen, Xiaoyu Shi, Ye Pan, and Zhengyang Xu

Abstract—Magnetoacoustic concentration tomography with magnetic induction (MACT-MI) is a noninvasive imaging method that reconstructs the concentration image of magnetic nanoparticles (MNPs) based on the acoustic pressure signal generated by the magnetic properties of MNPs. The performance of MNPs is of great significance in MACT-MI. To study influences of the uniaxial anisotropy of MNPs on MACT-MI, firstly, based on the static magnetization curve, the force characteristic that the MNPs with uniaxial anisotropy experienced was analyzed. The magnetic force equation with the space component separated from the time term was deduced. The acoustic pressure equation containing the concentration of the MNPs with uniaxial anisotropy was derived. Then, a two-dimensional axisymmetric simulation model was constructed to compare magnetic force, acoustic source, and acoustic pressure before and after considering the uniaxial anisotropy of MNPs. The effect of scanning angle and detection radius of ultrasonic transducer on the acoustic pressure was studied. Finally, the concentration image of the MNPs with uniaxial anisotropy was reconstructed by the time reversal method and the method of moments (MoM). Theoretical considerations and simulation results have shown that the magnetic force has a triple increase after taking into account the uniaxial anisotropy of MNPs. The take-off time of acoustic pressure waves is only related to the position of the uniaxial anisotropy MNPs region. From the reconstructed image, concentration distribution and spatial location and size information of the uniaxial anisotropy MNPs region can be distinguished. The research results may lay the foundation for MACT-MI in subsequent experiments and even clinical applications.

1. INTRODUCTION

Magnetic nanoparticles (MNPs) with biocompatibility, microsize effect, and good magnetic guidance can achieve drug delivery through magnetic regulation and have been widely used in biomedical fields [1–3]. Research on noninvasive imaging technology is of crucial importance for detecting the distribution characteristics of MNPs *in vivo* and realizing microscopic diagnosis and treatment.

Magnetic particle imaging (MPI) is a tracer method based on tomographic imaging technology to detect the spatial distribution of MNPs [4–7]. In 2005, the first MPI scanner was designed and developed by Gleich and Weizenecker [8]. In 2012, they presented the first micromagnetic de novo simulation of anisotropic MNPs spectra and found MPI strongly depends on the anisotropy of MNPs [9]. In 2015, Graeser et al. proposed the constructive superposition of MNPs shape and MNPs crystal anisotropy resulted in the best performance in MPI sensitivity and resolution [10]. In 2016, they demonstrated that the signal of anisotropic MNPs was not based on MNPs parameters such as size and shape alone but was also determined by the field sequence that MNPs experience at their spatial position [11].

Received 12 July 2021, Accepted 11 November 2021, Scheduled 23 November 2021

* Corresponding author: Yuxin Hu (hu_yu_xin@foxmail.com).

The authors are with the Faculty of Electrical and Control Engineering, Liaoning Technical University, Huludao, Liaoning 125105, China.

In 2017, Orendorff et al. provided that the MPI can be applied to imaging traumatic brain injury events with excellent contrast [12]. In 2018, Wang et al. used MPI to image islet phantoms and islet transplanted [13]. In the same year, Jung et al. utilized a new theranostic platform, which can be used to deliver anticancer drugs and radiosensitizers to various hypoxic cancers while using MPI to image the therapeutic effects [14]. In 2019, Ota et al. proved that MNPs structure with large core diameter and anisotropy plays an important role in the large amplitude and high resolution of MPI signals [15]. In the same year, Zhao et al. indicated that the type of magnetocrystalline anisotropy had a significant effect on the MPI performance of MNPs [16]. In 2020, Makela et al. reported that MPI provided quantitative information on *in vivo* iron labeling of macrophages [17]. To address physical limitations of MPI, an alternative method magnetoacoustic concentration tomography with magnetic induction (MACT-MI) is explored. The acoustic signal generated by the vibration of MNPs in the gradient magnetic field is detected to reconstruct MNPs concentration images. In 2020, Shi et al. deduced the equation between magnetic force and MNPs concentration based on the assumption of isotropy of MNPs in Langevin theory [18]. In 2021, Yan et al. used Maxwell-Helmholtz coil to saturate MNPs. Compared with unsaturated magnetized MNPs, the saturated magnetized MNPs had stronger magnetic force [19]. They adopted the method of moments (MoM) to reconstruct the concentration distribution and proposed that there is a negative correlation between the quality of the reconstructed image and the radius of the imaging target [20].

So far, the research of MACT-MI was based on the isotropy hypothesis of MNPs in Langevin theory. However, due to contributions such as magnetocrystalline, shape, and surface, MNPs exhibited anisotropy, and the anisotropy displayed a first order-dominant uniaxial characteristic [21]. The magnetization of MNPs was affected by many factors [22–26], among which the uniaxial anisotropy of MNPs directly led to the change of the static magnetization curve [27]. In the numerical calculation, magnetic force, acoustic source, and acoustic pressure were all solved based on the static magnetization curve. If the assumption of isotropy was still used, large errors would be introduced. Therefore, the MACT-MI simulation research on the uniaxial anisotropy of MNPs was carried out. A mathematical-physical model of the relationship between acoustic source and concentration of the MNPs with uniaxial anisotropy was constructed. The influences on MACT-MI before and after considering the uniaxial anisotropy of MNPs were analyzed and compared. The variation law of magnetic force of MNPs in excitation waveform, concentration, and magnetic field gradient was studied. Furthermore, the effect of scanning angle and detection radius of ultrasonic transducer on the acoustic pressure was analyzed. Finally, the time reversal method and MoM were applied to reconstruct the concentration distribution of the MNPs with uniaxial anisotropy.

2. METHOD

2.1. Principle of Tomography

The principle of MACT-MI is shown in Figure 1. A z direction gradient magnetic field is induced by two pulse currents in opposite directions passing through Maxwell coils. When MNPs are exposed to a time-varying magnetic field, they will be subjected to magnetic force, causing acoustic vibration in the tissue. The acoustic signal generated by the vibration is detected by an ultrasonic transducer. The MNPs concentration distribution is reconstructed in light of the nonlinear correlation determined between the acoustic signal and concentration.

2.2. Method of Tomography

2.2.1. Static Magnetization Curve of MNPs

Consider that an MNP composed of a superparamagnetic material, including a core responsible for its magnetic behavior and a magnetically neutral coating that prevents agglomeration of the MNPs [28, 29]. Neglecting the anisotropy of MNPs, the static magnetization curve of MNPs with isotropy can be represented by Langevin function $L(\alpha)$ as indicated in Figure 2. The equilibrium magnetization reads

$$\mathbf{M}(\mathbf{H}) = NmL(\alpha)\,\mathbf{e}_H \tag{1}$$

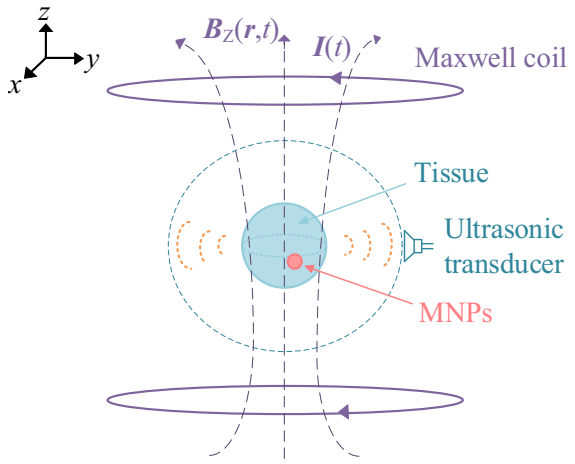

Figure 1. Schematic diagram of MACT-MI.

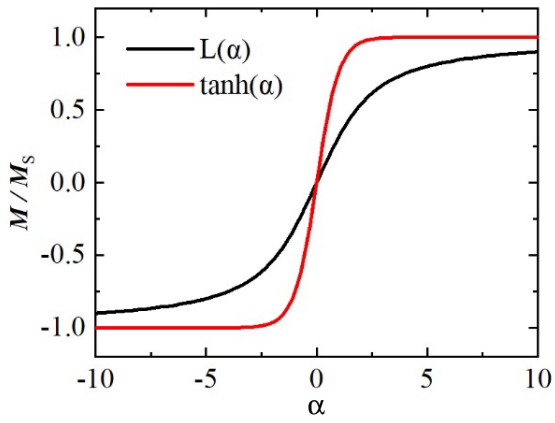

Figure 2. Static magnetization curves of the MNPs with isotropic and the MNPs with uniaxial anisotropy.

where N is the number of MNPs per unit volume; $L(\alpha) = \coth\alpha - 1/\alpha$, $\alpha = \mu_0 mH/kT$; μ_0 is the permeability in vacuum; $m = \|\mathbf{m}\|_2$ is the magnitude of the inherent magnetic moment; $H = \|\mathbf{H}\|_2$ is the magnetic field strength; k is the Boltzmann constant; and T is the temperature.

The widely performed Langevin theory intrinsically ignores the anisotropy of MNPs. Due to contributions such as shape, surface, and magnetocrystalline, the anisotropy can be complex. However, one of these contributions dominates and determines the main first-order contribution. From the perspective of an MNP, it can be usually concluded from experimental studies that anisotropy exhibits a first-order dominant uniaxial characteristic [21]. In fact, uniaxial anisotropy is a universal property of MNPs, and it is of great significance to study the influence of the uniaxial anisotropy of MNPs on MACT-MI.

MNPs with uniaxial anisotropy behave similarly to a two-level model. The magnetic moment m of a single MNP can only point in positive or negative z-direction which differs from the situation in Langevin theory where any direction is allowed. The easy axes of MNPs with uniaxial anisotropy can be aligned using magnetic field [30, 31]. The static magnetization curve can be represented by Hyperbolic tangent function $\tanh(\alpha)$ as depicted in Figure 2. The equilibrium magnetization is expressed

$$\mathbf{M}(\mathbf{H}) = Nm\tanh(\alpha)\,\mathbf{e}_H \tag{2}$$

Compared with the static magnetization curve of the MNPs with isotropic based on Langevin theory, the static magnetization curve of the MNPs with uniaxial anisotropy has a steeper slope and stronger magnetization characteristics. The magnetization curve of MNPs affects the magnetic force, acoustic source, and acoustic pressure. Therefore, the uniaxial anisotropy of MNPs cannot be neglected in the MACT-MI research.

2.2.2. Analysis of the Forward Problem

Consider the MNPs with uniaxial anisotropy as magnetic dipoles [32]. When gradient magnetic field is applied, MNPs experience the magnetic force which can be expressed as

$$\mathbf{f} = \mathbf{m} \cdot \nabla \mathbf{B} \tag{3}$$

Assume that N represents the MNPs concentration in the tissue. The magnetic force $\mathbf{F}$ is described as

$$\mathbf{F} = \int_0^N \mathbf{f} dN = \int_0^N \mathbf{m} \cdot \nabla \mathbf{B} dN \tag{4}$$

Since $\mathbf{m}$ is the symmetric about z axis, its components in the plane perpendicular to $\mathbf{B}$ cancel each other, and only the z component m_z remains after integration. Therefore, the magnetic force is described as

$$\mathbf{F} = \frac{\partial B_z}{\partial z}\mathbf{e}_z \int_0^N m_z dN = \mathbf{M}(\mathbf{H}) \frac{\partial B_z}{\partial z}\mathbf{e}_z \tag{5}$$

For the MNPs with uniaxial anisotropy, substituting Equation (2) into Equation (5), the magnetic force can be expressed as

$$\mathbf{F} = Nm\tanh(\alpha) \frac{\partial B_z}{\partial z}\mathbf{e}_z \tag{6}$$

According to the parameter settings in this paper, $\tanh(\alpha) \approx \alpha$, Equation (6) can be simplified to

$$\mathbf{F} = N\frac{m^2}{kT} B_z \frac{\partial B_z}{\partial z}\mathbf{e}_z \tag{7}$$

Assuming that the imaging target is located in the near field of the magnetic source, and B_z can be described as the product of spatial and temporal components

$$B_z(\mathbf{r}, t) = B_z(\mathbf{r})\, g(t) \tag{8}$$

where $B_z(\mathbf{r})$ is the spatial component of the magnetic field, and $g(t)$ is the temporal component of the magnetic field.

Substituting Equation (8) into Equation (7), the equation can be converted into

$$\mathbf{F}(\mathbf{r}, t) = N\frac{m^2}{kT} B_z(r) \frac{\partial B_z(r)}{\partial z} g^2(t)\mathbf{e}_z \tag{9}$$

Establish the active linear acoustic pressure equation

$$\nabla^2 p - \frac{1}{c_s^2}\frac{\partial^2 p}{\partial t^2} = \nabla \cdot \left[N\frac{m^2}{kT} B_z(r) \frac{\partial B_z(r)}{\partial z}\mathbf{e}_z\right] g^2(t) \tag{10}$$

where p is the acoustic pressure, and c_s is the velocity of acoustic in tissue.

At initial moment before the Maxwell coils is energized, and the imaging target has no gradient magnetic field. The MNPs with uniaxial anisotropy have no magnetic force. When there is no acoustic source, the initial conditions are

$$\begin{cases} p|_{t=0^-} = 0 \\ \left.\dfrac{\partial p}{\partial t}\right|_{t=0^-} = 0 \end{cases} \tag{11}$$

The original acoustic field generated by the acoustic vibration is $p(\mathbf{r}, t)$. Due to the characteristics of the ultrasonic transducer, it has an impulse response function $h(t)$. The acoustic pressure output by the ultrasonic transducer is described as

$$w(\mathbf{r}, t) = p(\mathbf{r}, t) \otimes h(t) + n(t) \tag{12}$$

where $n(t)$ is the noise signal.

2.2.3. Analysis of the Inverse Problem

In the frequency domain, Equation (12) can be described as

$$W(\mathbf{r}, \omega) = P(\mathbf{r}, \omega) \otimes H(\omega) + n(\omega) \tag{13}$$

where $W(\mathbf{r}, \omega)$, $P(\mathbf{r}, \omega)$, $H(\omega)$, and $n(\omega)$ represent the Fourier spectrum functions of $w(\mathbf{r}, t)$, $p(\mathbf{r}, t)$, $h(t)$, and $n(t)$, respectively.

According to least mean-variance calculation and the Wiener filter deconvolution, the original acoustic field at the detection point of the ultrasonic transducer is

$$p(\mathbf{r}, t) = \mathrm{FFT}^{-1}\left(\frac{W(\mathbf{r}, \omega) H(\omega)}{|H(\omega)|^2 + C}\right) \tag{14}$$

where FFT^{-1} is the inverse Fourier transform; $C = 1/(a\,|H(\omega)|)$, a is used to match the ratio change of the noise power spectrum and the input signal during the entire period. The acoustic pressure $W(\mathbf{r},\omega)$ detected by the ultrasonic transducer is deconvolved by Wiener filter through Equation (14) to obtain the original acoustic pressure $p(\mathbf{r},t)$.

Using the time reversal method, the acoustic source in the acoustic field inverse problem is

$$\nabla\cdot\mathbf{F}(\mathbf{r},t) = -\frac{1}{2\pi c_s^3}\oint_{\Sigma} dS_d \frac{\mathbf{n}\cdot(\mathbf{r}_d-\mathbf{r})}{|\mathbf{r}-\mathbf{r}_d|^2}\, p''\left(\mathbf{r}_d, |\mathbf{r}_d-\mathbf{r}|/c_s + t\right) \tag{15}$$

where $\mathbf{r}_d$ is the position of ultrasonic transducer on the measuring surface Σ, and $\mathbf{n}$ is the unit outward normal of the measuring surface Σ.

Equation (9) indicates that the magnetic force has only z direction. Therefore

$$\nabla\cdot\mathbf{F}(\mathbf{r},t) = \frac{\partial}{\partial z}F_z(\mathbf{r},t) \tag{16}$$

According to Equation (16), combining the initial conditions to perform the inverse divergence expansion of the magnetic force divergence, the magnetic force $\mathbf{F}(\mathbf{r},t)$ can be obtained. Substituting Equation (9) can reconstruct the concentration distribution of the MNPs with uniaxial anisotropy.

2.3. Numerical Simulation

In the simulation, to verify the correctness of the magnetic force equation based on the MNPs with uniaxial anisotropy, a pair of Maxwell coils was used to generate a z direction time-varying gradient magnetic field. The magnetic field intensity near the axis was

$$B_z = \frac{\mu_0 nIR^2}{2\sqrt{\left(R^2+\left(z+\frac{\sqrt{3}R}{2}\right)^2\right)^3}} - \frac{\mu_0 nIR^2}{2\sqrt{\left(R^2+\left(z-\frac{\sqrt{3}R}{2}\right)^2\right)^3}} \tag{17}$$

where the number of coil turns $n = 3$; the coil radius $R = 150\,\mathrm{mm}$; the radius of the coil cross-section was $5\,\mathrm{mm}$; the lower coil was set at the space $z = 0\,\mathrm{mm}$; the conductivity of the coil was set to $6\times10^7\,\mathrm{S/m}$.

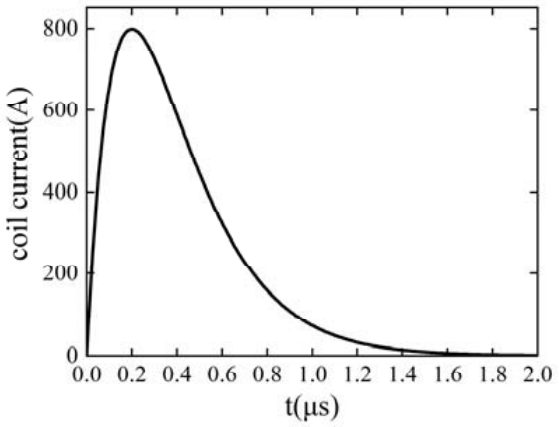

Figure 3. The waveform of the applied current.

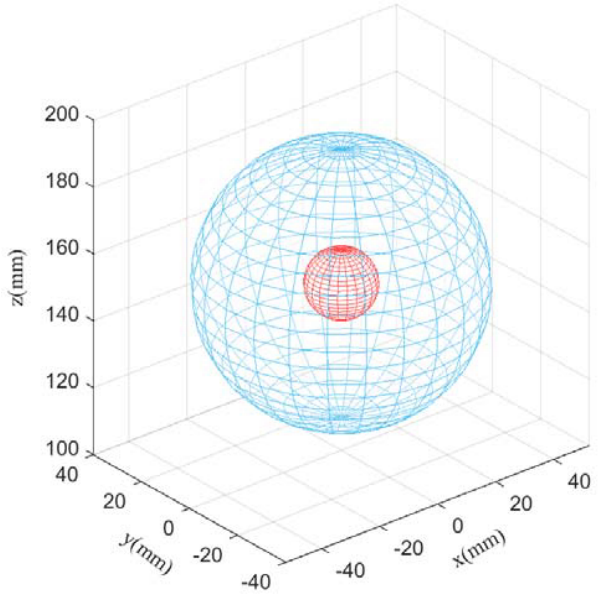

Figure 4. Two-dimensional axisymmetric simulation model.

The time characteristic of the current I is given in Figure 3. The current reached its peak value at 0.2 μs, and the period was 2 μs, i.e., the frequency was 500 kHz. At this frequency, the change in the magnetic dipoles interaction caused by the change of MNPs concentration can be ignored [33]. The two-dimensional axisymmetric simulation model was constructed in COMSOL Multiphysics as illustrated in Figure 4. The outer sphere represented the tissue with a radius of 40 mm, and the inner sphere represented the uniaxial anisotropy MNPs region with a radius of 5 mm. Because the Maxwell coils would produce a field free point in the central area, the center of the concentric sphere was set at (0, 0, 150) mm. The concentration of MNPs was 4×10^{20} particles/m^3 [34]. The permeability μ of the MNPs with uniaxial anisotropy was a diagonal matrix. Since the magnetic field generated by the Maxwell coils had only z direction in the research object, μ could be regarded as a scalar. The parameters of the MNPs with uniaxial anisotropy are shown in Table 1.

Table 1. Simulation parameters.

Parameter	Variable	Value
Boltzmann constant	k	1.38×10^{-23} J/K
Temperature	T	300 K
Particle diameter	d	10 nm
Saturation magnetization	M_S	0.6/μA/m
Vacuum permeability	μ	$4\pi \times 10^{-7}$
Particle volume	$V = \pi d^3/6$	
Magnetic moment	$m = VM_S$	

With the help of a magnetic field module, the magnetic field in the space was calculated, and the magnetic force that the MNPs with uniaxial anisotropy experienced was solved by Equation (9). With the aid of the acoustic field coupling module, the uniaxial anisotropy MNPs region was set as the dipole domain source and set as the magnetic force in Equation (9). The acoustic pressure Equation (10) and the initial condition Equation (11) were combined to solve the acoustic pressure and study the space-time characteristics of the acoustic field of the MNPs with uniaxial anisotropy. The scanning path of the ultrasonic transducer is presented in Figure 5. The rotation angle and detection radius were set to perform circular scanning, and the acoustic signal at different detection points was collected. The convolutional acoustic pressure signal based on Equation (12) was calculated. According to the acoustic field inverse problem, the original acoustic field was obtained by deconvolution of the acoustic

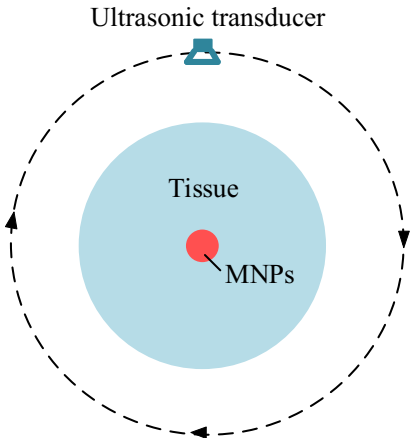

Figure 5. The scanning path of the ultrasonic transducer.

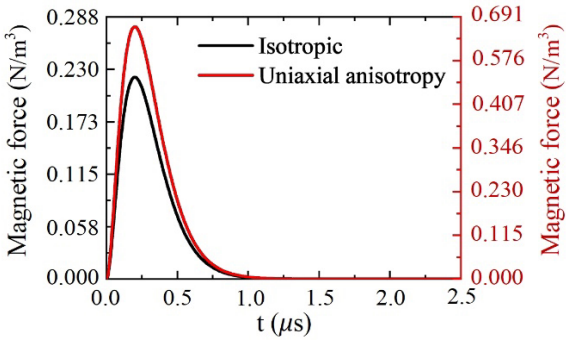

Figure 6. The magnetic force before and after considering the uniaxial anisotropy of MNPs.

pressure signal output by the ultrasonic transducer using Wiener filter based on Equation (14). The time reversal method was used to substitute the second derivative matrix of the inverted acoustic field into Equation (16) to obtain the acoustic source of the MNPs with uniaxial anisotropy in the imaging target. Using the differential method, adding boundary conditions, the magnetic force was calculated based on the magnetic field inverse problem. The MoM was used to reconstruct the concentration distribution of the uniaxial anisotropy MNPs region in the imaging target according to Equation (9).

3. RESULTS

Take the central point (0, 0, 150) mm where the uniaxial anisotropic MNPs region is located. The magnetic force responses before and after considering the uniaxial anisotropy of MNPs are plotted in Figure 6. When the same pulse current is applied, it can be seen that the magnetic force generated by the MNPs with uniaxial anisotropy is triple that of the MNPs with isotropy. The magnetization curve of the MNPs with scanning and the acoustic signal at different detection points are depicted. The convolutional acoustic pressure signal based on Equation (12) was calculated. According to the acoustic field uniaxial anisotropy has a steeper slope and stronger magnetization characteristics, thereby exciting a stronger magnetic force, which proves the influence of MNPs with uniaxial anisotropy on the magnetic force.

The normalized acoustic source on the $z = 140 \sim 160$ mm axis where the MNPs region is located is taken and plotted in Figure 7. Biological tissues are characterized by weak diamagnetism, low conductivity, weak scattering, and small changes in acoustic velocity and density. MNPs have high magnetic properties. Therefore, the acoustic field in space is mainly produced by MNPs. As depicted in Figure 7, the position of the sudden change of acoustic source is the position of the boundary of MNPs region. In the same pulse excitation conditions, the uniaxial anisotropic MNPs region has significantly stronger acoustic source amplitude than the isotropic MNPs region. To obtain a more accurate acoustic source, the uniaxial anisotropy of MNPs cannot be neglected.

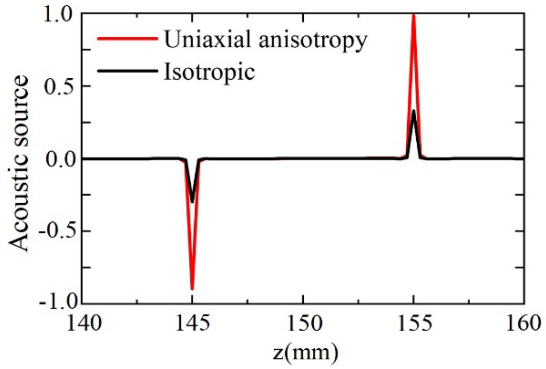

Figure 7. $z = 140 \sim 160$ mm, acoustic source before and after considering the uniaxial anisotropy of MNPs.

As elucidated in Figure 8, before and after considering the uniaxial anisotropy of MNPs, the acoustic field distributions of the YOZ section at 0.01 µs are taken. It can be seen that the acoustic field characteristics of MNPs are consistent with the physical characteristics of acoustic dipoles. The propagation characteristics of the acoustic field caused by the force source conform to the acoustic pressure equation of dipoles. Since $t = 0.01$ µs is close to the moment when the MNPs begin to produce an electromagnetic response, the acoustic wave only propagates outward from the acoustic source in one direction. In the direction of force, the phase of the acoustic wave is the opposite. After the uniaxial anisotropy of MNPs is considered, the acoustic pressure is stronger, which further proves the influence of the uniaxial anisotropy of MNPs on MACT-MI.

With a spatial step length of 0.5 mm, the 21 points on the geometric axis $z = 145 \sim 155$ mm of the uniaxial anisotropy MNPs region are scanned. At the same time, with a time step length of

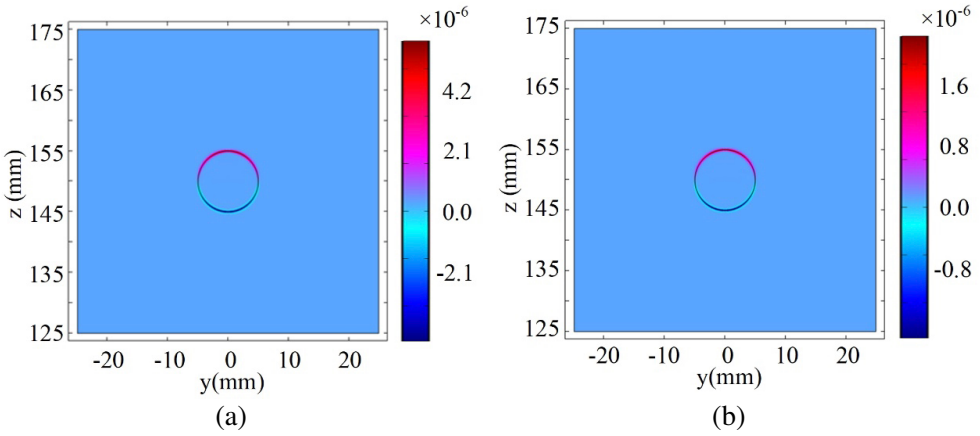

Figure 8. $t = 0.01\,\mu s$, acoustic field distribution (a) after considering the uniaxial anisotropy of MNPs, (b) before considering the uniaxial anisotropy of MNPs.

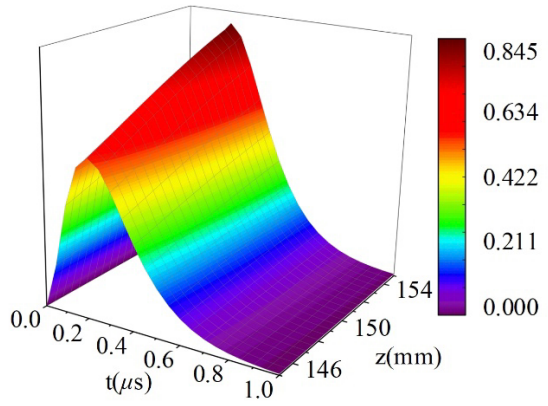

Figure 9. The magnetic force varies with $t = 0 \sim 1\,\mu s$ and $z = 145 \sim 155\,mm$.

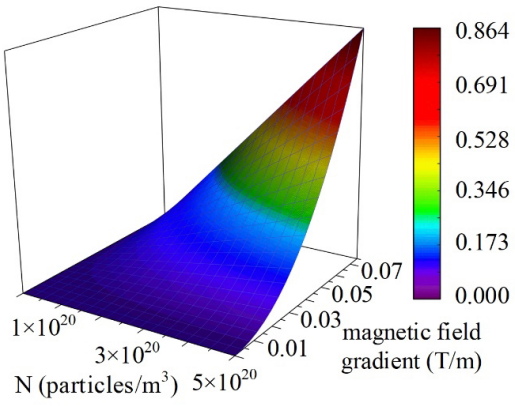

Figure 10. The magnetic force varies with magnetic field gradient $0 \sim 0.075\,T/m$ and concentration $0 \sim 5 \times 10^{20}$ particles/m^3.

0.05 μs, the 21 points within the time $0 \sim 1\,\mu s$ are scanned. The magnetic force is calculated according to Equation (9). As illustrated in Figure 9, the magnetic force is positively related to the coordinate position. As the coordinate position approaches the Maxwell coil, the intensity of the magnetic field increases, and the magnetic force on the MNPs with uniaxial anisotropy becomes stronger. The response waveform change at each point on the intercept line is consistent with the excitation waveform.

With a step length of $0.0015\,T/m$, the 51 points in the range of $0 \sim 0.075\,T/m$ of the magnetic field gradient are scanned. At the same time, with a step length of 0.1×10^{20} particles/m^3, the 51 points in the range of $0 \sim 5 \times 10^{20}$ particles/m^3 of the concentration are scanned. The magnetic force on the MNPs with uniaxial anisotropy at (0, 0, 150) mm is calculated according to Equation (9). As depicted in Figure 10, the magnetic force has a linear relationship with the concentration and a quadratic positive correlation with the magnetic field gradient. When the concentration is greater than 1×10^{20} particles/m^3 and the magnetic field gradient greater than $0.03\,T/m$, the magnetic force of the MNPs with uniaxial anisotropy gradually increases. When the magnetic field gradient changes rapidly, the magnetic force rises significantly, which helps to enhance the signal strength and facilitate the signal acquisition.

The detection radius of the ultrasonic transducer is set to $r_d = 10$, 20, and 30 mm, and the detection point in the 90° direction is placed at (0, 0, 160) mm, (0, 0, 170) mm, and (0, 0, 180) mm, respectively. The normalized time characteristic curve of the acoustic field at these three points is

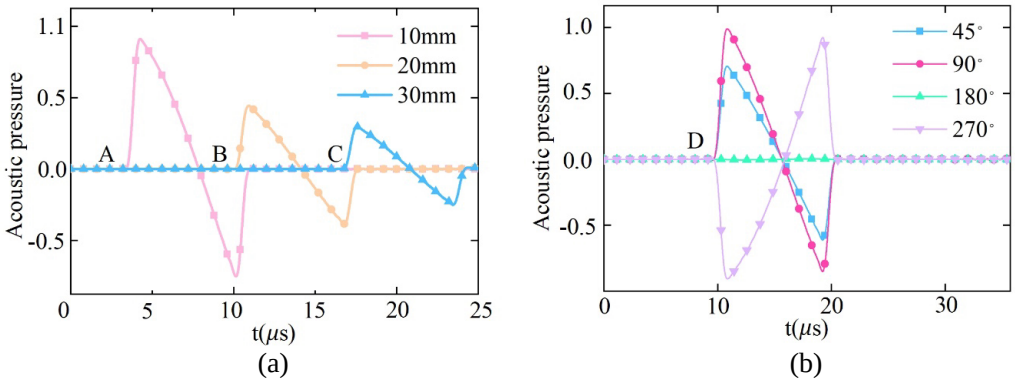

Figure 11. Time characteristic curve of acoustic field (a) different detection radius, (b) different detection angles.

represented in Figure 11(a). The take-off position of the wave cluster corresponds to the propagation time of the acoustic wave from the boundary point (0, 0, 155) mm of the uniaxial anisotropic MNPs region to the three detection points. The corresponding propagation distances are $d = 5$ mm, 15 mm, and 25 mm. Biological tissue is similar to fluid, and the propagation speed of acoustic waves in the tissue is 1500 m/s. The theoretical calculation time is 3.33 μs, 10 μs, and 16.67 μs, corresponding to the actual simulation time $t_A = 3.3$ μs, $t_B = 10$ μs, and $t_C = 16.7$ μs in Figure 11(a). When a point acoustic source propagates in a homogeneous medium, the acoustic wave takes the form of a spherical wave centered on the acoustic source. Due to diffusion, the acoustic intensity attenuates as the propagation distance increases; therefore, the acoustic intensity at point A in the figure is the largest, and point C is the smallest.

With the (0, 0, 150) mm point in the uniaxial anisotropic MNPs region as the center, the detection radius of the ultrasonic transducer is set to 20 mm, and the scanning angle is set to 45°, 90°, 180°, and 270°, respectively. The normalized time characteristic curves of the acoustic field at these three points are depicted in Figure 11(b). Acoustic pressure is the integral of the acoustic source on an arc with a radius of propagation distance. The corresponding acoustic sources on the arcs with different scanning angles are different. It can be seen that the 90° integral is positive; 270° is in the opposite phase; and the integral is negative. The acoustic signal propagates in the z direction, and the detection acoustic signal in the vertical direction, which is 180°, is close to 0. The take-off time of the acoustic wave is the time when the acoustic wave propagates from the position of the nearest uniaxial anisotropy MNPs region to the detection point. The spatial position information of the uniaxial anisotropic MNPs region can be obtained by using the curve of the acoustic wave.

The MNPs with uniaxial anisotropy concentrations are respectively taken as 2×10^{20}, 4×10^{20}, and 6×10^{20} particles/m^3. The detection point radius of the ultrasonic transducer is set to 20 mm, and the scanning angle is 90°. The normalized acoustic field characteristic curve is plotted in Figure 12. $t_{B1} = 10$ μs is still the time for the acoustic wave to propagate from the boundary point (0, 0, 155) mm of the uniaxial anisotropic MNPs region to the detection point. It can be seen that the acoustic wave take-off time is only related to the position of the uniaxial anisotropic MNPs region. Increasing the concentration can enhance the amplitude of the acoustic signal and facilitate the acquisition of the acoustic signal.

The concentration distribution in the 50×50 mm imaging target is calculated. According to the method of moments, the finite element meshing method is used to discretize the imaging target into 240×240 element blocks. The concentration distribution of the MNPs with uniaxial anisotropic in imaging target is taken at $t = 0.012$ μs. The reconstructed image in Figure 13(a) is compared with the concentration distribution in the target model in Figure 13(b). Due to the influence of the projection calculation of the time reversal method, there will be artifacts corresponding to the excitation current pulse width at the boundary. However, the effective boundary position information and the spatial size of the uniaxial anisotropic MNPs region can still be reflected, which fully proves the feasibility and correctness of the forward problem model.

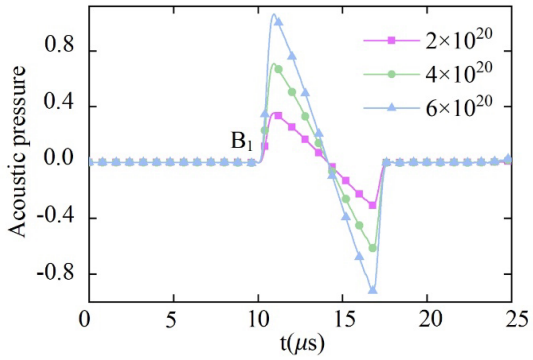

Figure 12. Acoustic fields of MNPs with different concentration.

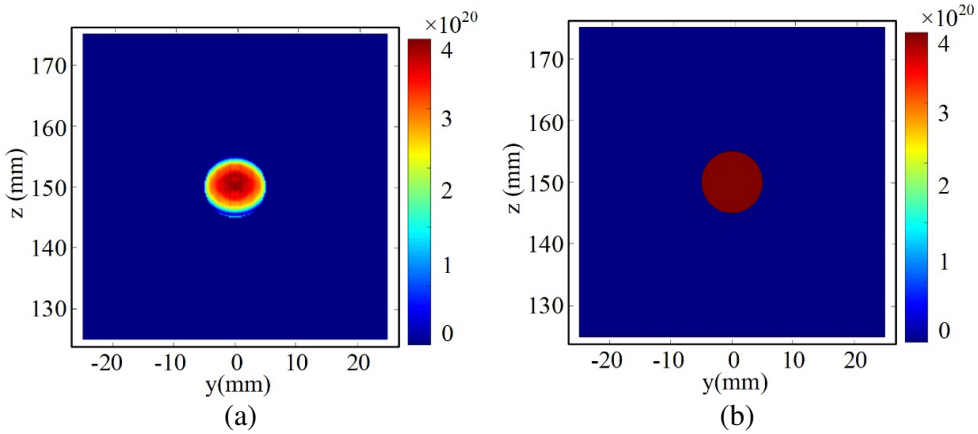

Figure 13. Concentration image. (a) is the reconstructed MNPs concentration. (b) is the target MNPs concentration. The circular region represents the MNPs region. The square represents the imaging background.

4. CONCLUSION AND DISCUSSION

In this paper, theoretical analysis and numerical simulation were used to study MACT-MI on uniaxial anisotropy of MNPs. The main conclusions are as follows:

(1) In the same external gradient magnetic field conditions, compared with the MNPs with isotropic based on Langevin theory, the magnetic force generated by the MNPs with uniaxial anisotropy is greater. A greater magnetic force can excite a stronger acoustic signal. The uniaxial anisotropy of MNPs affects the magnetic force, acoustic source, and acoustic pressure, which verifies the effect of the uniaxial anisotropy of MNPs on MACT-MI. To obtain a more accurate acoustic source, the uniaxial anisotropy of MNPs cannot be neglected;

(2) The magnetic force of the MNPs with uniaxial anisotropy has the same time characteristic as the excitation waveform, which is proportional to the concentration and linearly related to the magnetic field gradient. Increasing the concentration and magnetic field gradient can enhance the amplitude of the acoustic signal, which is conducive to signal acquisition;

(3) Extracting the acoustic field characteristic curves of different parameter detection points, the take-off time of the acoustic wave is only related to the position of the uniaxial anisotropic MNPs region. Using the acoustic curve, the spatial position information of the uniaxial anisotropic MNPs region can be obtained, which verifies the feasibility of the theory;

(4) The reconstructed concentration image reflects the effective boundary position information and the space size of the uniaxial anisotropic MNPs region, which fully proves the feasibility and correctness of the forward problem model.

MACT-MI is a noninvasive imaging method that can quantitatively detect MNPs. So far, the research of MACT-MI is based on the assumption of isotropy of MNPs. Due to contributions such as magnetocrystalline, shape, and surface, MNPs exhibit uniaxial anisotropy, which affects the physical process of MACT-MI. Therefore, based on the uniaxial anisotropy of MNPs, it is possible to obtain more realistic and accurate magnetic force, acoustic source, and acoustic pressure.

Based on the uniaxial anisotropy of MNPs, we have obtained magnetoacoustic signals with a higher signal-to-noise ratio, but there is a lack of experiments to further study the magnetization, magnetic force, acoustic source, and acoustic pressure. In future research, experimental research should be carried out to verify MACT-MI systems theory. The research in this paper is based on the premise that the media is uniform in acoustic, ignoring the influence of acoustic parameters on the propagation of magnetoacoustic. For the subsequent exploration of MACT-MI, the influence of acoustic inhomogeneity should be further considered. In the simulation, it is not accurate to set the sound velocity to a fixed value, and the attenuation of the sound wave is not considered. Therefore, the simulation model needs to be further optimized. MACT-MI is based on the assumption of equilibrium conditions, and it is instructive to study the equilibrium case before moving on to nonequilibrium cases. Future work is expected to study the influence of the dynamic magnetization properties of MNPs on MACT-MI. It should be considered that larger MNPs may show dynamic magnetic relaxation effects. For example, the Brownian rotation of larger MNPs can be impacted by the viscosity of the particle suspension, hydrodynamic volume of MNPs, and temperature, resulting in a significant influence in magnetic forces and acoustic source, which might be additional relevant factors in selecting optimal MNPs and magnetic fields. In summary, an in-depth study on MACT-MI based on the uniaxial anisotropy of MNPs has been conducted in this paper. The basic theory of MACT-MI is improved, which provides the basis for further experiments and clinical research of MACT-MI.

ACKNOWLEDGMENT

This research was supported by the Natural Science Foundation of Liaoning Province (No. 2019-ZD-0039) and the Basic Research Project fundation from Liaoning Education Department, China (No. LJ2020JCL003).

REFERENCES

1. García-Jimeno, S., R. Ortega-Palacios, M. F. Cepeda-Rubio, A. Vera, L. Leija-Salas, and J. Estelrich, "Improved thermal ablation efficacy using magnetic nanoparticles: A study in tumor phantoms," *Progress In Electromagnetics Research*, Vol. 128, 229–248, 2012.
2. Zhu, X., J. Li, P. Peng, N. Hosseini-Nassab, and B. R. Smith, "Quantitative drug release monitoring in tumors of living subjects by magnetic particle imaging nanocomposite," *Nano Lett.*, Vol. 19, 6725, 2019.
3. Trujillo-Romero, C. J., S. Garcia-Jimeno, A. Vera-Hernandez, L. Leija-Salas, and J. Estelrich, "Using nanoparticles for enhancing the focusing heating effect of an external waveguide applicator for oncology hyperthermia: Evaluation in muscle and tumor phantoms," *Progress In Electromagnetics Research*, Vol. 121, 343–363, 2011.
4. Zheng, B., et al., "Quantitative magnetic particle imaging monitors the transplantation, biodistribution, and clearance of stem cells *in vivo*," *Theranostics*, Vol. 6, 291–301, 2016.
5. Yu, E. Y., et al., "Magnetic particle imaging: A novel *in vivo* imaging platform for cancer detection," *Nano Lett.*, Vol. 17, 1648, 2017.
6. Zhou, X. Y., et al., "Magnetic particle imaging for radiation-free, sensitive and high-contrast vascular imaging and cell tracking," *Curr. Opin. Chem. Biol.*, Vol. 45, 131, 2018.
7. Wu, L. C., et al., "A review of magnetic particle imaging and perspectives on neuroimaging," *Am. J. Neuroradiol.*, Vol. 40, 206, 2019.
8. Gleich, B. and J. Weizenecker, "Quantitative drug release monitoring in tumors of living subjects by magnetic particle imaging nanocomposite," *Nature*, Vol. 435, 1214, 2005.

9. Weizenecker, J., B. Gleich, J. Rahmer, and J. Borgert, "Micro-magnetic simulation study on the magnetic particle imaging performance of anisotropic mono-domain particles," *Phys. Med. Biol.*, Vol. 57, 7317, 2012.
10. Graeser, M., K. Bente, and T. M. Buzug, "Dynamic single-domain particle model for magnetite particles with combined crystalline and shape anisotropy," *J. Phys. D: Appl. Phys.*, Vol. 48, 275001, 2015.
11. Graeser, M., K. Bente, A. Neumann, and T. M. Buzug, "Trajectory dependent particle response for anisotropic mono domain particles in magnetic particle imaging," *J. Phys. D: Appl. Phys.*, Vol. 49, 045007, 2016.
12. Orendorff, R., et al., "First *in vivo* traumatic brain injury imaging via magnetic particle imaging," *Phys. Med. Biol.*, Vol. 62, 3501, 2017.
13. Wang, P., et al., "Magnetic particle imaging of islet transplantation in the liver and under the kidney capsule in mouse models," *Quant. Imaging Med. Surg.*, Vol. 8, 114, 2018.
14. Jung, K. O., H. Jo, J. H. Yu, S. S. Gambhir, and G. Pratx, "Development and MPI tracking of novel hypoxia-targeted theranostic exosomes," *Biomaterials*, Vol. 177, 139, 2018.
15. Ota, S., et al., "Effects of size and anisotropy of magnetic nanoparticles associated with dynamics of easy axis for magnetic particle imaging," *J. Magn. Magn. Mater.*, Vol. 474, 311, 2019.
16. Zhao, Z., N. Garraud, D. P. Arnold, and C. Rinaldi, "Effects of particle diameter and magnetocrystalline anisotropy on magnetic relaxation and magnetic particle imaging performance of magnetic nanoparticles," *Phys. Med. Biol.*, Vol. 65, 025014, 2020.
17. Makela, A. V., J. M. Gaudet, M. A. Schott, O. C. Sehl, C. H. Contag, and P. J. Foster, "Magnetic particle imaging of macrophages associated with cancer: Filling the voids left by iron-based magnetic resonance imaging," *Mol. Imaging Biol.*, Vol. 22, 958, 2020.
18. Shi, X., G. Liu, X. Yan, and Y. Li, "Simulation research on magneto-acoustic concentration tomography of magnetic nanoparticles with magnetic induction," *Comput. Biol. Med.*, Vol. 119, 103653, 2020.
19. Yan, X., Y. Pan, W. Chen, Z. Xu, and Z. Li, "Simulation research on the forward problem of magnetoacoustic concentration tomography for magnetic nanoparticles with magnetic induction in a saturation magnetization state," *J.Phys. D: Appl. Phys.*, Vol. 54, 075002, 2021.
20. Yan, X., Z. Xu, W. Chen, and Y. Pan, "Implementation method for magneto-acoustic concentration tomography with magnetic induction (MACT-MI) based on the method of moments," *Comput. Biol. Med.*, Vol. 128, 104105, 2021.
21. Carrey, J., B. Mehdaoui, and M. Respaud, "Simple models for dynamic hysteresis loop calculations of magnetic single-domain nanoparticles: Application to magnetic hyperthermia optimization," *J. Appl. Phys.*, Vol. 109, 083921, 2011.
22. Halgamuge, M. N. and T. Song, "Optimizing heating efficiency of hyperthermia: Specific loss power of magnetic sphere composed of superparamagnetic nanoparticles," *Progress In Electromagnetics Research B*, Vol. 87, 1–17, 2020.
23. Miclaus, S., M. Racuciu, and P. Bechet, "H-field contribution to the electromagnetic energy deposition in tissues similar to the brain but containing ferrimagnetic particles, during use of face-held radio transceivers," *Progress In Electromagnetics Research B*, Vol. 73, 49–60, 2017.
24. Miclaus, S., C. Iftode, and A. Miclaus, "Would the human brain be able to erect specific effects due to the magnetic field component of an UHF field via magnetite nanoparticles?," *Progress In Electromagnetics Research M*, Vol. 69, 23–36, 2018.
25. Rusakov, V. V., et al., "Nonlinear magnetic response of a viscoelastic ferrocolloid: Effective field approximation," *Colloid J.*, Vol. 83, 116, 2021.
26. Das, P., et al., "Colloidal polymer-coated Zn-doped iron oxide nanoparticles with high relaxivity and specific absorption rate for efficient magnetic resonance imaging and magnetic hyperthermia," *J. Colloid Interface Sci.*, Vol. 579, 391, 2020.

27. Mamiya, H. and B. Jeyadevan, "Nonequilibrium magnetic response of anisotropic superparamagnetic nanoparticles and possible artifacts in magnetic particle imaging," *PLoS One*, Vol. 10, e0118156, 2015.
28. Gupta, A. K. and M. Gupta, "Synthesis and surface engineering of iron oxide nanoparticles for biomedical applications," *Biomaterials*, Vol. 26, 3995, 2005.
29. Kus, M., F. Ozel, N. M. Varal, and M. Ersoz, "Luminescence enhancement of OLED performance by doping colloidal magnetic FE_3O_4 nanoparticles," *Progress In Electromagnetics Research*, Vol. 134, 509–524, 2013.
30. Kötitz, R., et al., "Determination of the binding reaction between avidin and biotin by relaxation measurements of magnetic nanoparticles," *J. Magn. Magn. Mater.*, Vol. 194, 62, 1999.
31. Ekaterina, A., O. Alexey, and J. Philip, "Static magnetization of immobilized, weakly interacting, superparamagnetic nanoparticles," *Nanoscale*, Vol. 11, 21834, 2019.
32. Li, Y., Q. Ma, D. Zhang, and R. Xia, "Acoustic dipole radiation model for magnetoacoustic tomography with magnetic induction," *Chin. Phys. B.*, Vol. 20, 084302, 2011.
33. Ota, S., T. Yamada, and Y. Takemura, "Dipole-dipole interaction and its concentration dependence of magnetic fluid evaluated by alternating current hysteresis measurement," *J. Appl. Phys.*, Vol. 117, 17D713, 2015.
34. Brandl, M., M. Mayer, J. Hartmann, T. Posnicek, C. Fabian, and D. Falkenhagen, "Theoretical analysis of ferromagnetic microparticles in streaming liquid under the influence of external magnetic forces," *J. Magn. Magn. Mate.*, Vol. 322, 2454, 2011.